Estimating the Oceanic Kinetic Energy Cascade from Along-Track Altimetry

Oscar Vergara
Collecte Localisation Satellites (CLS)
Jonathan Gula
Université de Brest https://orcid.org/0000-0002-0876-9557
René Schubert (schubert.rene@t-online.de)
University of Brest, CNRS, IRD, Ifremer, Laboratoire d'Océanographie Physique et Spatiale (LOPS), IUEM
https://orcid.org/0000-0003-1118-3968

Article

Keywords:

Posted Date: June 19th, 2023

DOI: https://doi.org/10.21203/rs.3.rs-2924613/v1

Additional Declarations: There is **NO** Competing Interest.

Estimating the Oceanic Kinetic Energy Cascade from Along-Track Altimetry

René Schubert[1,*], Oscar Vergara[2] and Jonathan Gula[1,3]

[1]University of Brest, CNRS, IRD, Ifremer, Laboratoire d'Océanographie Physique et Spatiale (LOPS), IUEM, Brest, France
[2] Collecte Localisation Satellites (CLS), Ramonville Saint-Agne, France
[3] Institut Universitaire de France (IUF), France
*corresponding author, rene.schubert@univ-brest.fr

The oceanic kinetic energy cascade, the flux of kinetic energy between currents of different horizontal scales, shapes the structure of the global ocean circulation and associated heat, salt, nutrient, and oxygen fluxes. Here, we show with two numerical ocean simulations that the surface geostrophic cascade can be estimated from satellite altimetry observations and present for the first time its regional distribution and seasonal cycle at scales of 40 to 150 km for large parts of the global ocean on the basis of observations. The time-mean cascade is inverse (towards larger scales), strongest in large-scale current systems and decreases with distance from these systems. In the open ocean, the inverse cascade is associated with a maximum in late winter at the smallest scales studied, which transitions to scales larger than 100 km within two to three months, consistent with the widespread absorption of mixed-layer eddies by mesoscale eddies in spring.

1 Introduction

Ocean motions can be decomposed into movements at different horizontal scales ranging from large-scales ($\mathcal{O}$(1000 km)) through mesoscales ($\mathcal{O}$(100 km)) and submesoscales ($\mathcal{O}$(100 m) – $\mathcal{O}$(10 km)) to microscales (<$\mathcal{O}$(100 m)). The flux of kinetic energy (KE) between ocean currents at different scales, the KE cascade, plays a key role in several aspects of global climate. First, in combination with the transformation of KE into available potential energy (and vice versa), the cascade mediates the balance between the oceans forcing by the atmosphere, primarily by wind at large scales, and the dissipation of KE into heat at molecular scales[1]. Second, the KE cascade controls the scale-distribution of KE including the strength of the subtropical gyre[2], the strength and position of large-scale currents such as the Gulf Stream[3,4], the strength of inter-ocean exchanges such as Agulhas leakage[5], and the strength and distribution of ocean mesoscale eddies[6–8] and thus the associated transports of heat, salt, nutrients, and oxygen. Third, through ocean-atmosphere interactions, the ocean and atmosphere KE cascades determine their response times to external forcing[9]. This induces a modulation of the atmospheric circulation by the oceanic KE cascade. In addition to being a key component of the climate system, understanding the KE cascade is critical for the validation and development of climate models, particularly regarding the parameterization of the sub-grid-scale energetic fluxes and dissipation.

For the large mesoscales, the KE flux can be computed from gridded sea-surface height data that were interpolated from along-track satellite altimetry measurements on a regular 0.25° and daily grid (AVISO) assuming geostrophy and an f-plane[6,10,11]. The results show at these scales an inverse cascade from smaller to larger scales. At scales of the maximum inverse flux (about 200 km), the cascade has been shown to be orders of magnitude smaller in the open ocean compared to regions of strong current systems[12]. This is not surprising, as the inverse cascade is stopped in the open ocean at smaller scales due to for example the Rhines effect[13]. Substantial inverse fluxes occur at these scales only in the large-scale current systems, where very large mesoscale eddies form as a consequence of large-scale instabilities and interact with the large-scale currents. Regional submesoscale-permitting simulations and regional observations showed that the inverse cascade extends into the submesoscales to scales of the mixed-layer Rossby radius of deformation (about 15 km)[11,14–19]. Applying for the first time a filtering approach for the computation of the KE flux[20–23] to submesoscale-permitting model data, it was found that the underlying process of the submesoscale inverse cascade is primarily the absorption of submesoscale mixed layer eddies by mesoscales eddies[16]. Consistently, the maximum of the submesoscale inverse flux has been found to occur immediately after the submesoscale season in late winter and to shift within a few months towards larger scales in spring[16]. Based on observations, the existence of the submesoscale inverse KE cascade and its seasonality could only be demonstrated for small ocean regions[15,17–19]. Indirect evidence that this submesoscale inverse cascade is active in large parts of the global ocean has recently been provided by high-resolution satellite products[24]. Recent model studies have applied Helmholtz decomposition and principal strain coordinate transformation prior to the computation of the scale KE flux, and have shown that the inverse cascade is primarily driven by geostrophically balanced flows[25,26]. This confirms that it should be possible to analyze the near-surface inverse KE cascade on the basis of sea-surface height.

In this study, we provide for the first time an observation-based estimate of the surface geostrophic KE cascade and its seasonal cycle at scales of 40-150 km in large parts of the global ocean. For this purpose, we use information on the dynamics in the respective scale-band from satellite along-track altimetry data measured by JASON-3 as well as from two submesoscale-permitting simulations of the Atlantic. The KE flux can not be computed directly from along-track sea-surface height. With the simulations we prove that it is however possible to estimate the KE flux from the simulated sea-surface height along the tracks of JASON-3 and apply the proposed estimation technique to the actual measurements.

2 Results

If the measured along-track absolute dynamic topography (η) is dominated by geostrophic flows, the across-track f-plane geostrophic flow component can be computed as $u = -\frac{g}{f}\eta_y$, where $g = 9.81$ m s^{-2} is the gravitational acceleration, $f = 2\Omega\sin(2\pi\frac{\theta}{360^\circ})$ is the Coriolis parameter with the Earth's angular speed $\Omega = \frac{2\pi}{86400}$ s^{-1} and the latitude θ, and y is the along-track direction with increasing latitude. Partial derivatives of a with respect to b are written here and in the following as $\frac{\partial a}{\partial b} = a_b$. For this study, we use five years of tide-corrected and filtered measurements of η taken by the JASON-3 satellite along the tracks shown in Figure 1a. From these, we estimate the surface geostrophic $5^\circ \times 5^\circ$ domain-averaged scale-KE flux through a specific scale L as

$$\langle \Pi_{est} \rangle^L = -C(L)\rho_0 \langle \overline{u^2}^L - \overline{u}^L \overline{u}^L \rangle \langle |\overline{u}^L_y| \rangle, \tag{1}$$

where angle brackets indicate averages over $5^\circ \times 5^\circ$ subdomains for each measurement cycle, C is an estimation coefficient identified from a numerical ocean simulation, and $\rho_0 = 1024$ kg m^{-3} is the standard density. The overlines denote fields convolved with a tophead kernel whose length is equal to that of the respective scale L and which is normalized so that it integrates to 1. The computation of C and the proof that the proposed estimation works is given in section 3.

2.1 The time-mean scale KE flux

The time-mean estimated fluxes at scales of 60, 140 and 200 km are shown in Figure 1. The largest (inverse) fluxes occur at all scales in regions of very strong near-surface current systems, such as the Gulf-Stream (GS) - North-Atlantic-Current (NAC) system, the Agulhas system, the Brazil-Malvinas-Confluence (BMC) or the Kuroshio. The further away from the large-scale currents, the smaller the fluxes. Fluxes at 140 km and 200 km scales are very close to each other and have substantial amplitudes almost only in regions of large-scale current systems. At 200 km, the pattern is very similar to the one presented in a previous study based on gridded AVISO data[12]. At this scale, almost no time-mean fluxes are found in the open ocean. At 60 km, fluxes of about 10-20 mW km^{-1} m^{-3} occur in large parts of the mid-latitudes. This is consistent with wide-spread mixed-layer instabilities leading to the formation of submesoscale eddies, which are subsequently absorbed by the mesoscales[16].

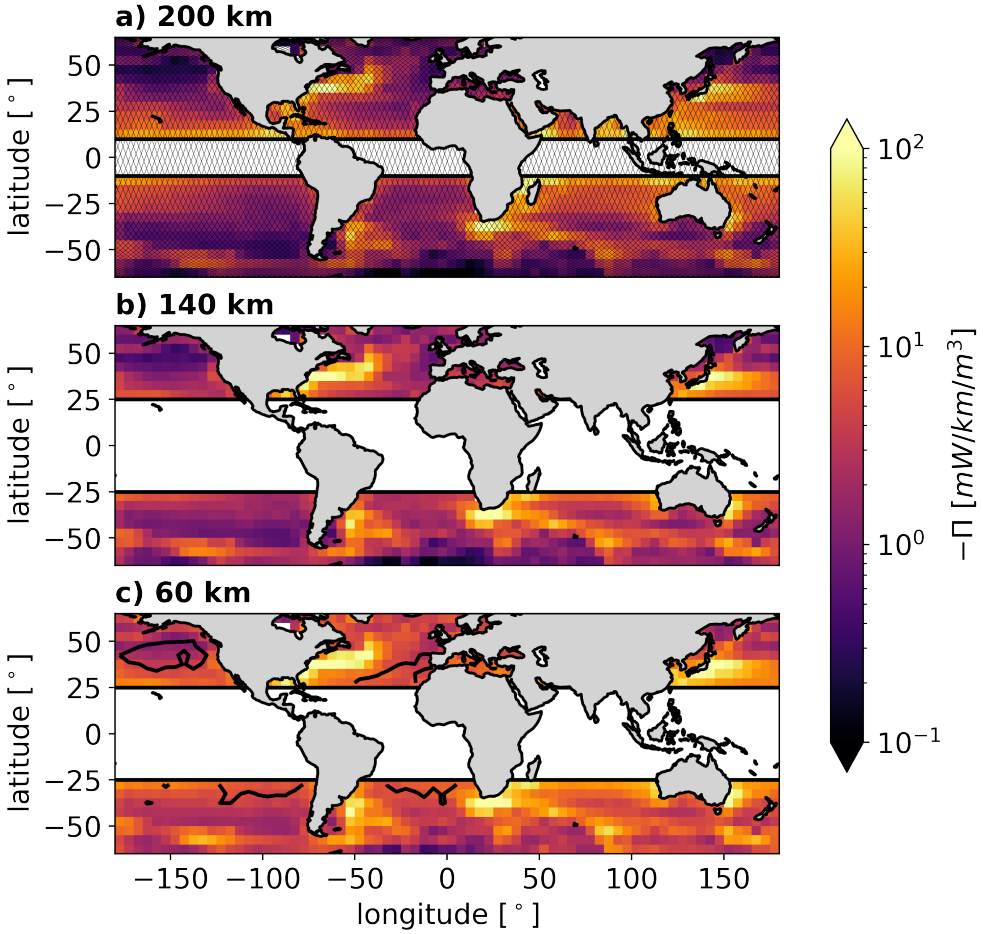

Figure 1. *The time-mean $-\Pi_{est}$ from JASON-3 at scales of 200 km (**a**), 140 km (**b**), and 60 km (**c**). In **a**), thin black lines show the JASON-3 tracks. In **c**), black contours mark regions where the time-mean transition scale from balanced to unbalanced flows T is larger than 60 km and thus, where the results have to be interpreted with care.*

2.2 The seasonal cycle of the scale KE flux

The seasonal cycle of Π_{est} and its scale-distribution is shown in Figure 2. At 60 km, the anomalies of the FMA-mean (Fig. 2a) and the ASO-mean (Fig. 2b) relative to the 2017-2021 mean flux show enhanced inverse fluxes in spring and reduced inverse fluxes in autumn for most open ocean regions. This is consistent with a previously published map of the seasonal difference in geostrophic KE computed from along-track altimetry[24]. In the open ocean, enhanced fluxes occur in winter and spring with a maximum in early spring (February in the Northern Hemisphere and June in the Southern Hemisphere) at 40 km scale (Fig. 2c and 2d). During the following three months, enhanced fluxes occur at increasingly larger scales. Deeper mixed layer depths in winter allow for the accumulation of more available potential energy at mixed-layer fronts. Mixed-layer baroclinic instability of the fronts releases this potential energy into KE in the form of mixed-layer eddies[24]. These eddies have a diameter on the order of the mixed-layer Rossby deformation radius (about 15 km) and are stronger and more frequent in winter. Subsequently, these eddies grow and are absorbed by mesoscale eddies. The absorption process takes about 2-3 months, resulting in a shift of the maximum scale KE flux from late winter at 30 km to late spring at 140 km. This climatological scale-time pattern of the observation-based estimated inverse flux is consistent with that of the power-spectral density of KE computed from AVISO[27] and along-track altimetry[24]. The same consistency was also found in a simulation of the open ocean near the Agulhas-system[16]. In regions of strong large-scale flows, in particular the GS and Kuroshio extensions, the BMC, and the Agulhas region and Return Current, the estimated fluxes at 60 km mainly show an opposite seasonal cycle to that of the open ocean. This is consistent with results from a recent model study of the Gulf Stream, which found a stronger seasonal cycle of the balanced cascade outside of the Gulf Stream core, including a scale-shift of the maximum inverse flux and a reduced seasonality without a scale-shift of the maximum in a region that partially includes the Gulf Stream[25]. Furthermore this is consistent with previously published results on along-track altimetry based geostrophic KE levels, which revealed an opposite

seasonal cycle within the strong current-systems[24]. We speculate that the reason for this phenomenon is that other energetic submesoscale and mesoscale processes overcome the seasonal cycle of mixed-layer instabilities and the subsequent inverse cascade of the resulting mixed layer eddies. In the future, it will be necessary to clarify what these other processes are and whether they have a seasonal cycle.

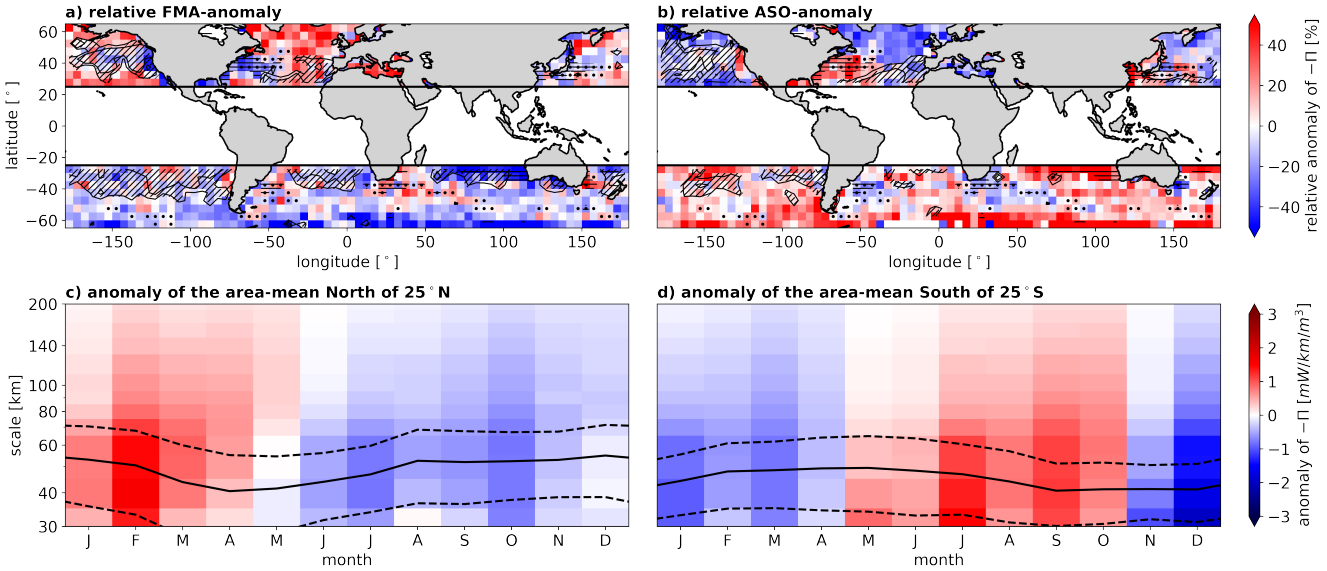

Figure 2. *Monthly climatological anomalies of* $-\Pi_{est}$ *with respect to the 2017-2021 mean. Red (blue) colors mark enhanced (reduced) inverse cascade. The top panels show the relative anomalies for the FMA-mean (**a**) and ASO-mean (**b**) flux at 60 km. The lower panels show the anomalies for the area-mean flux north of* $25°N$ *(**c**) and south of* $25°S$ *(**d**). Contour lines and hatches mark where the transition scale from balanced to unbalanced flows* T *is larger than 60 and 70 km and thus, where the results are potentially erroneous due to non-geostrophic gradients of* η*. Regions of strong large-scale currents are excluded before the area-averaging for the bottom panels. They are identified by temporal standard deviation of 2017-2021 AVISO-SSH averaged over* $5° \times 5°$ *domains that larger than 20 cm (dotted) and by anomalies of the KE flux that are larger than 5 mW* km^{-1} m^{-3} *at 60 km (horizontal hatches). In the bottom panels the respective area-mean* T *(solid line) plus and minus one standard deviation (dashed lines) are shown.*

2.3 The transition scale between balanced and unbalanced flows

If η is not dominated by geostrophic flows, the computation of geostrophic currents from the measurements fails. Away from strong current systems, there are also regions with an opposite seasonal cycle in the open ocean, such as the North East Pacific or the Central Atlantic. These are regions where a scale of 60 km is smaller than the maximum of the local transition scale from balanced to unbalanced flows T in the respective season (shown with contours and hatches in Fig. 2a and 2b). T is estimated from the JASON-3 along-track data with a previously published method[28] and is averaged over the same $5° \times 5°$ grid on which we estimate the scale KE flux. It provides a lower bound for the scales at which the respective gradients of η can be used to derive geostrophic flows. T is associated with a seasonal cycle with smaller values in spring, when there are more balanced submesoscale vortices and larger values in summer and autumn when the surface signature of internal waves is amplified[29] (lines in Fig. 2c and 2d). There are also large regional differences, with lower values in regions with strong balanced flows (large-scale currents and surface eddy path) and higher values in regions with weak balanced flows (weak eddy activity)[28]. In particular in summer, in regions of weak mesoscale activity at scales of 70 km and smaller, the measured absolute dynamic topography is not dominated by balanced flows and Π_{est} gives spuriously enhanced values. This is manifested in a spurious reduction or reversal of the seasonal cycle at 60 km in these regions (Fig. 2c and 2d) and small secondary maxima of Π_{est} in summer (August in the Northern Hemisphere and February in the Southern Hemisphere) mainly at scales smaller than 70 km (Fig. 2c and 2d). In Figures 1 and 2 we therefore highlight with black lines the regions, scales and seasons where the results are partially corrupted by too strong imprints of unbalanced flows into the absolute dynamic topography measurements. Furthermore, we exclude the tropics between $25°S$ and $25°S$ for our analysis, because the baroclinic mode-1 and mode-2 diurnal tides significantly affect the SSH-spectrum[30] there, and consequently T exceeds 75 km throughout the year[31].

3 Methods

3.1 JASON-3 satellite along-track altimetry data

JASON-3 measures the absolute dynamic topography η, the sum of the sea-level anomaly and the mean dynamic topography, between $66°S$ and $66°N$ with an along-track resolution of about 6 km at 1 Hz and a repeated measurement of each track every 10th day. Below scales of 25-35 km, JASON-class data are associated with noise[32,33]. This noise is associated with a seasonal cycle that is similar, but not identical, to that of the submesoscale KE level[33] (at least north of $40°S$[34]): higher noise and submesoscale KE in winter and lower in summer. The sea-level anomaly is available in an original (unfiltered) and a low-pass "filtered" version. Fourier-analysis shows that the seasonal cycle of power spectral density of the unfiltered η has deviations from 20 km on all scales larger than 30 km (Fig. 3e), indicating that the seasonal cycle at these scales is not corrupted by measurement noise. Furthermore, the corrections for the barotropic tides and the coherent part of the baroclinic tides for modes M2, K1, O1 and S2 are available and allow the reconstruction of the absolute dynamic topography including tides or with tidal correction applied. Note, however, that there is a residual effect of tides that cannot be corrected. Note also that η is the sea-surface height (SSH) corrected by the geoid. Since the geoid is associated with very large scales, this correction is not relevant for the analysis presented in this study. Therefore, η is also referred to as SSH in the following.

3.2 GIGATL1 simulations

The GIGATL1 simulations[35] used here have been performed with the Coastal and Regional Ocean COmmunity model (CROCO, 10.5281/zenodo.7415055), which is based on the Regional Ocean Modeling System (ROMS[36]). The integration is performed on an Arakawa C-grid[37] using 100 vertical terrain-following sigma-levels where the bathymetry is taken from the SRTM30plus dataset. Vertical mixing is parameterized with the k-epsilon turbulence closure scheme with applied Canuto A stability function. No explicit lateral diffusivities and viscosities are used. The effect of bottom friction is parameterized with a logarithmic law using a roughness length of 0.01 m. The GIGATL1 grid is orthogonal based on an oblique Mercator projection and designed to have nearly uniform spacing in both horizontal dimensions. The grid spacing varies from 1 km at the central longitude of the grid to 735 m at the west and east extremes of the grid. A simulation with a grid-spacing of about 3 km "GIGATL3" has been initialized in January 2004. Initialization fields and boundary conditions are from Simple Ocean Data Assimilation (SODA[38]). GIGATL1 is initialized from the restarts of GIGATL3 in July 2007 and integrated twice, one experiment with simulated tides and one experiment without simulated tides. All simulations are forced by hourly atmospheric forcing data from the Climate Forecast System Reanalysis (CFSR) with a bulk formulation and a stress correction approach to parameterize the surface ocean current feedback to the atmosphere[39]. Barotropic tidal forcing at the boundaries and tidal potential and self attraction from TPXO7.2 and GOT99.2b are applied to GIGATL3 and GIGATL1 with tides. In this study, we analyze snapshots every fifth day over the period April 2008 to March 2009 for both simulations.

3.3 Model Validation

The temporal standard deviation of SSH, computed from daily averages during Apr 2008 - Mar 2009 averaged onto the AVISO grid, shows similar large-scale patterns for GIGATL1 with and without tides and AVISO (Fig. 3a and 3b). The largest values occur in the region of the GS-NAC and BMC systems, moderate values in the surrounding ocean, as well as in the Agulhas ring path, the Azores Current, and the North Equatorial Counter Current, and low values above the shelves and in the central subtropical gyres. While the two GIGATL runs show very similar values, the simulated SSH variabilities are smaller than in the observations in the GS extension, the Brazil Current extension, and the Agulhas Ring Path, and larger north of 50°N. The standard deviation of SSH in the Northwest-Corner and the NAC are in remarkably good agreement. The too low simulated SSH variability in the Agulhas ring path is a result of the monthly boundary conditions applied at the southern boundary of the domain, which are not frequent enough to resolve the full variability of the energetic eddies drifting out of the Agulhas region into the Atlantic.

Time-mean horizontal wavenumber spectra computed from SSH at JASON-3 tracks in a $20° \times 20°$ domain in the open ocean show similar results for JASON-3 and GIGATL1 with and without tides (Fig. 3g). For comparison, the GIGATL1 SSH is extracted at the measurement locations of JASON-3 from model snapshots every fifth day. The SSH-spectra from GIGATL1 with tides and the unfiltered JASON-3 data including tides (dashed lines) show a very good agreement at scales larger than 60 km. At scales smaller than 60 km, the spectrum of the observations shows higher values compared to the simulation, which could be due to observational noise or unresolved processes. The spectrum of the filtered JASON-3 SSH follows that of the unfiltered down to 45 km, but with a shallower slope between 60 km and 45 km than in the simulation, which shows a k^{-4} slope down to 30 km. Applying the spectral computation to daily mean GIGATL1 fields instead of snapshots, and thus to fields that include only a small fraction of the tidal effect, results in a similar reduction at scales larger than 90 km as in the JASON-3 spectrum computed from the tide-corrected SSH. Consistently, the spectrum from snapshots of the non-tidal run shows a similar power spectral density to that from daily means of the tidal-run.

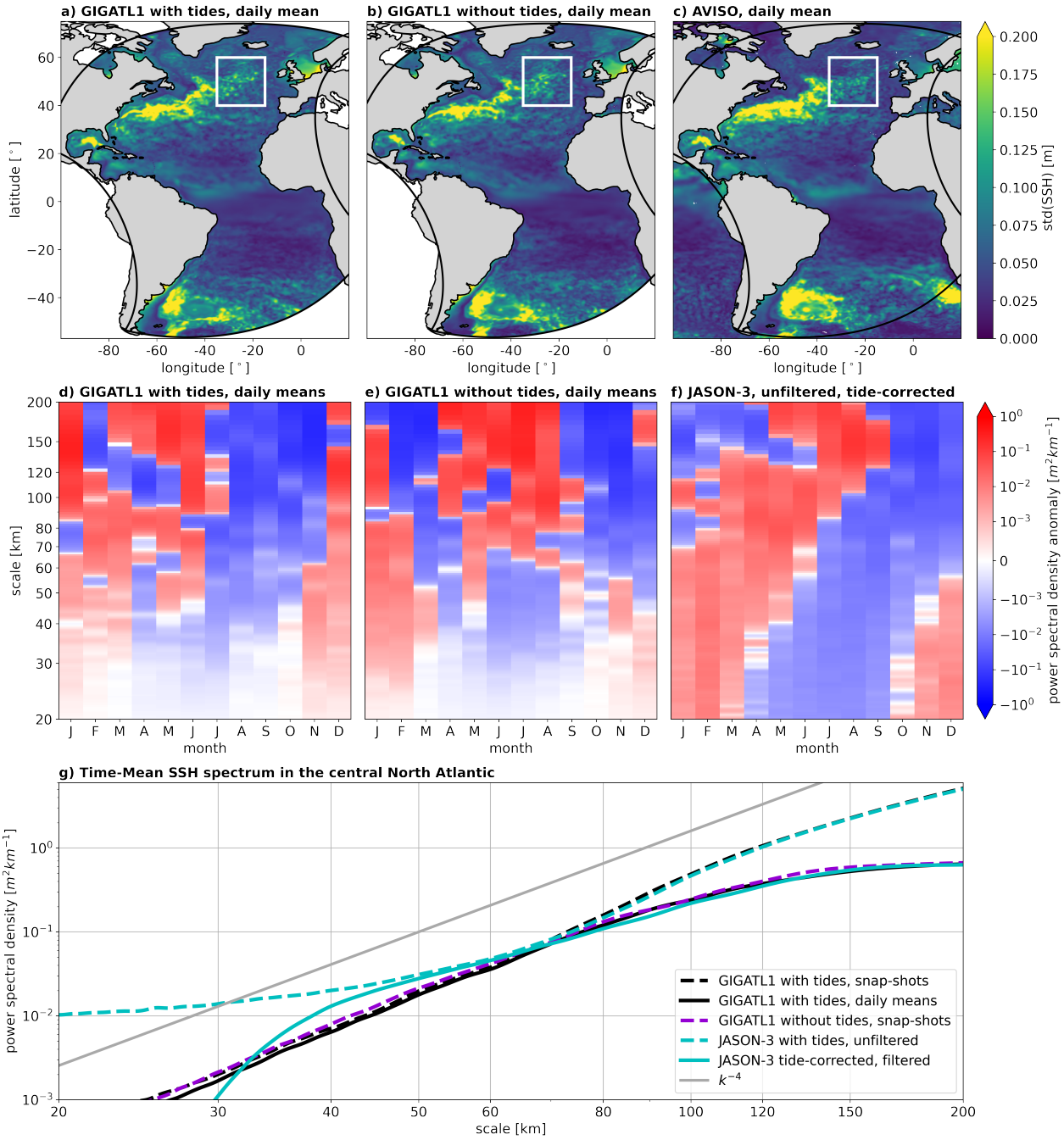

Figure 3. *The standard deviation of SSH computed from Apr 2008 - Mar 2009 daily mean fields of GIGATL1 with tides (**a**), GIGATL1 without tides (**b**), and AVISO (**c**). In the upper panels, thick black lines show the GIGATL1 domain, and the white box the region for which the Fourier-transform is performed for the middle and bottom panels. **d**), **e**), and **f**) show Hovmoeller-plots of the monthly climatological anomalies of the SSH spectra with respect to the mean over the period Apr 2008 - Mar 2009 for **d**) and **e**), and 2017-2021 for **f**). **g**) shows the time-mean SSH spectra and a gray straight line for the k^{-4} slope.*

Hovmoeller plots of the monthly climatology of the SSH-spectrum for both observations and simulations (Fig. 3d - 3f) show maxima that shift from winter at scales of $\mathcal{O}(10\,km)$ to summer at scales of $\mathcal{O}(100\,km)$ similar to the maximum inverse cascade estimated from JASON-3 (Fig. 2c). This shift is consistent with previous results from AVISO and simulations[16,27], as well as with a maximum of submesoscale activity in winter and spring and a subsequent inverse cascade involving the growth of submesoscale eddies and their absorption by mesoscale eddies[16].

3.4 The scale KE flux

With the filtering approach, the scale KE flux can be computed as

$$\Pi = -\rho_0[(\overline{u^2} - \overline{u}^2)\overline{u}_x + (\overline{uv} - \overline{u}\,\overline{v})(\overline{u}_y + \overline{v}_x) + (\overline{v^2} - \overline{v}^2)\overline{v}_y], \tag{2}$$

where u and v are the total horizontal velocity components in perpendicular directions x and y[20–22]. The overlines denote fields convolved with a two-dimensional top-head kernel whose diameter is equal to that of the respective scale L and which is normalized by the respective enclosed area so that it integrates to 1. Π is only computed if the full kernel area is filled with data. To reduce the memory requirement for convolutions in the computation of Π, which increases exponentially with the respective scale, u and v are first averaged within 5x5 grid-cell boxes. This has almost no effect on the results (not shown), as the variations of the simulated values on the near-grid-scale are very small. Due to limits in computational time and storage, the computations were only feasible for snapshots every fifth day. While this does not affect the results for area-averages, the results for time-averages may contain aliasing effects.

In both GIGATL1 runs, large amplitudes of surface time-mean Π occur mainly in regions of strong current systems (at 60 km scales shown in Fig. 4a and 4d). While the GS-NAC and BMC systems show time-mean fluxes of both signs, the equatorial current system is associated with a time-mean forward cascade. In addition, the tidal run shows enhanced time-mean forward fluxes in regions of strong internal tide generation (including the Azores, Cape Verde Islands, and the Guyot Province). Fluxes averaged over the region North of 25°N, show a dominant forward cascade in summer (JJAS) and a dominant inverse cascade in winter and spring (JFMA) (Fig. 4b and 4c). The summer forward cascade increases towards smaller scales and is much stronger in the tidal run compared to the non-tidal run. The maximum inverse cascade shifts by a few months with increasing scale. This is consistent with the absorption of the winter-time submesoscale vortices by the mesoscales, which that takes this time[16], and with the seasonal cycle of the SSH spectrum in the NAC (Fig. 3d and 3e).

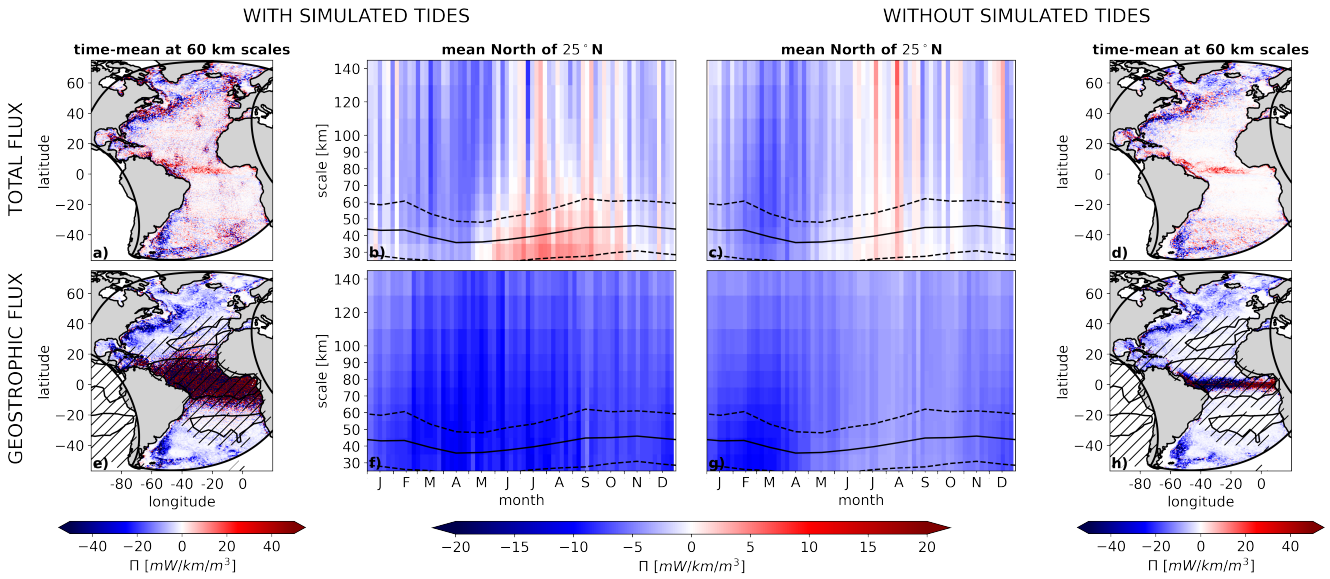

Figure 4. *The scale KE flux* Π *computed from the total (top) and the geostrophic (bottom) velocity from GIGATL1 with tides (left) and without tides (right) in the period Apr 2008 - Mar 2009. Hatches (contours) in* ***e)*** *and* ***h)*** *show, where the maximum (mean) of* T *is larger than 60 km. Lines in* ***b),c),f),*** *and* ***g)*** *show the area-mean* T *(solid) plus and minus one standard deviation (dashed).*

The geostrophic scale KE flux can be computed by using (2), with the geostrophic velocity. Noisy large-amplitude time-mean geostrophic fluxes occur in the tropics in the tidal run (Fig. 4e) and in the equatorial region in the non-tidal run (Fig. 4h). In the tidal run, the latitudional extent of the noisy fluxes decreases with increasing scale (not shown). Away from the noisy band, the time-mean geostrophic flux is inverse almost everywhere. Fluxes averaged North of 25°N, show a dominant inverse cascade at all times and scales as well (Fig. 4e and 4f). North of 25°N, the inverse cascade in both runs is maximum at the smallest investigated scales in February and March, which shifts to April and May at scales of 100 km and larger (Fig. 4f and 4g). The

similar timing and amplitude of the inverse cascade from the total velocity (Fig. 4b) support that balanced flows are primarily responsible for the inverse cascade, as shown in previous studies[25,26]. Furthermore this confirms that the near-surface winter and spring inverse cascade can be studied using SSH. However, for the interpretation of the geostrophic flux, one needs to be aware that the ageostrophic (net forward) cascade reduces the geostrophic (net inverse) cascade mainly at scales smaller than 40 km throughout the year (Fig. 4). Weaker minima of the flux occur at scales smaller than 70 km in JAS in the tidal run (Fig. 4f) that do not show up in the non-tidal run (Fig. 4g). These secondary minima result from non-geostrophic SSH-gradients and thus can not be interpreted as enhanced geostrophic fluxes. Finally, note that the results presented here for the surface cascade from total velocities correspond to an extreme case, as forward fluxes are surface intensified and restricted to the very upper ocean, while the inverse cascade driven by the balanced flows extends deep into the ocean[16,26] . The estimate for the geostrophic flux presented in section 2 is thus rather representative for the cascade spanning over the depth-range of surface intensified balanced flows than for the cascade directly at the surface.

3.5 Estimating the scale KE flux from along-track data

In order to access the smallest scales observed by satellite altimetry, we must use the non-gridded along-track SSH product. However, it is not possible to compute the geostrophic Π directly from along-track SSH, as one can only compute the across-track geostrophic velocity component. This implies that, of all the terms in (2), only the Leonard stress $\overline{u^2} - \overline{u}^2$, and the along-track derivative $\overline{u}_y$ are computable. For this study, we propose to estimate the flux with equation (1), which includes the product of these two terms giving the correct unit of a scale KE flux. Since $\overline{u^2} - \overline{u}^2$ is always positive, using the $|\overline{u}_y|$ along with the minus sign means that the estimated geostrophic flux is globally inverse, consistent with what we found for the time- and area-averaged geostrophic fluxes in the simulations (Fig. 4). We average both subterms over $5^\circ \times 5^\circ$ boxes, as the estimation works better the larger this region is (not shown), and as they are large enough to cover reasonable amounts of along-track data (which have a track-to-track distance of several degrees for ascending and descending tracks, Fig. 1a). The estimation coefficient C is identified from the simulations for each chosen scale ([30,40,50,60,70,80,90,100,120,140,160,180,200] km) by area- and time-averaging the term $\langle\Pi\rangle/(-\rho_0\langle\tau_{uu}\rangle\langle|\overline{u}_y|\rangle)$, where $\langle\Pi\rangle$ is computed from the 5x5 grid-cell averaged SSH field and the divisor terms from the SSH extracted from the simulation along the JASON-3 tracks. For the final area-averaging of the term, regions near the coast and boundary of the simulation, where the respective $5^\circ \times 5^\circ$ domain includes only a small ocean area are excluded (shown white in Fig. 6a), as well as regions and times where $L < T$. The resulting C is presented for each scale in Figure 5 and shows an exponential decay from 0.32 at 30 km to 0.10 at 200 km for the tidal-run. C is very similar for the non-tidal run. This means that we can use these values regardless of how much tidal effects are included in the observations. As the tide-corrected observations include only a small remaining tidal effect (namely the one of incoherent baroclinic tides that remains after $5^\circ \times 5^\circ$ averaging), we use the values of C identified from the non-tidal run in equation (1) and thus for the results presented in section 2.

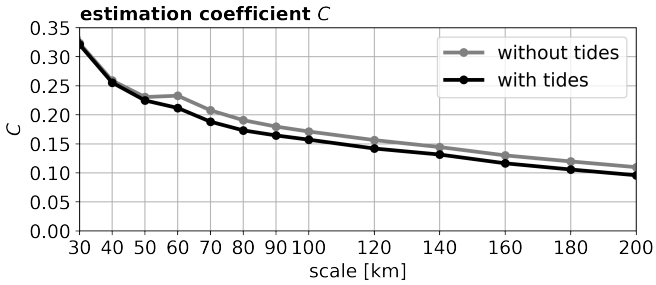

Figure 5. *The estimation coefficient C identified from the GIGATL1 simulations as a function of the scale L.*

Comparisons of the original and estimated time-mean fluxes at 60 and 140 km and of the original and estimated area-mean North of $25^\circ N$ (for regions that are not dotted in Figure 6a) for GIGATL1 with tides show that the estimation reproduces the horizontal and scale-time patterns and their amplitudes reasonably well even if the full tidal signal is included in the SSH (Fig. 6). At 60 km, differences mainly show up in the GS-NAC system and in regions where $T > 60$ km, where the flux is overestimated (Fig. 6c). Most of these differences are reduced at 140 km, except in the region of the GS east of its separation (Fig. 6f). The pattern and amplitude of the estimated fluxes from GIGATL1 with tides at 60 and 140 km are very close to those estimated from JASON-3 data (Fig. 1). However, for the observations, higher fluxes are estimated in the GS extension, the northern BMC, and the Agulhas ring path, which is consistent with higher mesoscale eddy activity in the observations (Fig. 3a and 3c).

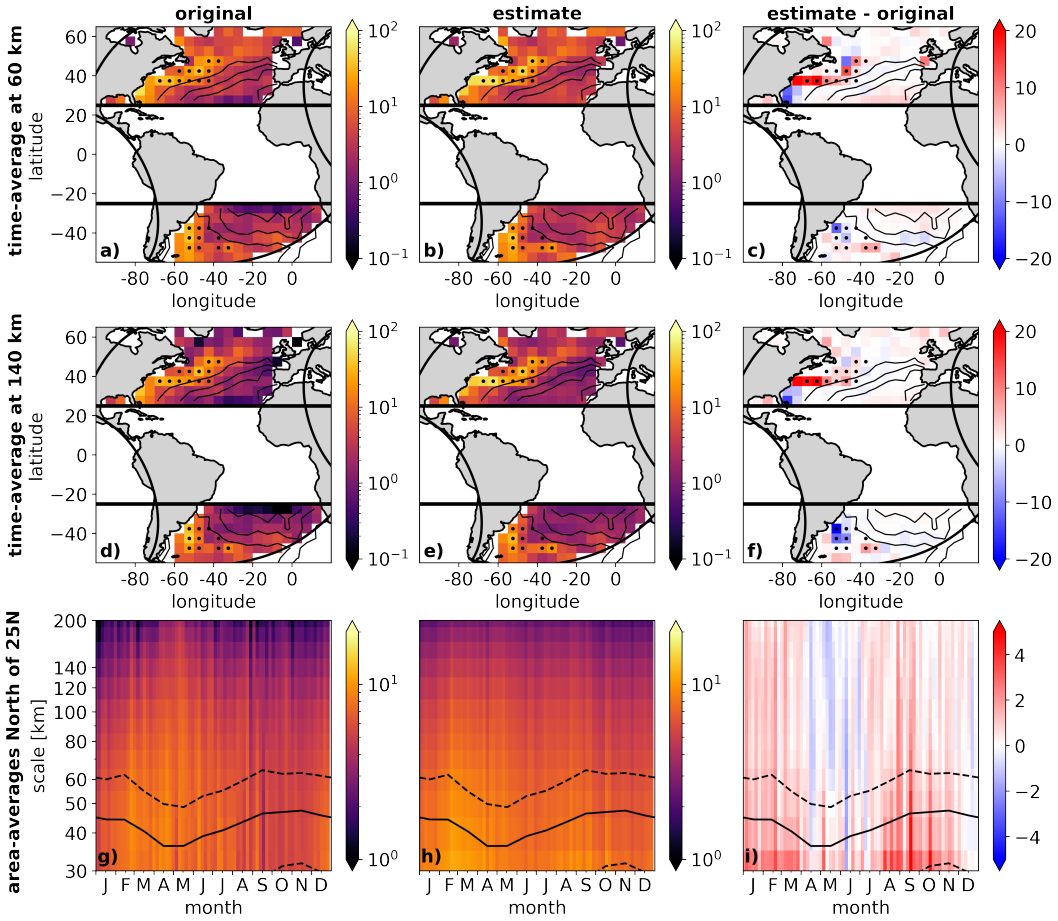

Figure 6. *The original and the estimated time-mean $-\Pi$ at 60 km (top) and 140 km (middle), as well as the area-mean in the regions North of 25°N that are not dotted in panel **a)** (bottom). All values are given in units of $mW/km/m^3$. Dotted regions show where the $5^\circ \times 5^\circ$ averaged standard deviation of the AVISO-SSH in 2017-2021 is larger than 20 cm. Contour lines in the top-panels mark where T is 40, 50, and 60 km. In the bottom panels, black lines show the respective area-mean T (solid) plus and minus one standard deviation (dashed). The differences of the estimate minus the original $-\Pi$ are shown on the right hand side, where blue colors mark underestimation and red overestimation.*

The largest differences between the area-averaged original and estimated geostrophic Π are found at scales smaller than 50 km in September, where the inverse cascade is overestimated (Fig. 6i). This is the season, where the transition scale is particularly large. This contributes to a reduced amplitude of the seasonal cycle of the estimated flux compared to the original flux, which can also be seen in the relative anomaly of spring (FMA) and autumn (ASO) means relative to the annual mean (Fig. 7). In most regions with $T < 40$ km, the inverse cascade is enhanced in spring, while it is weaker in autumn. Regions with $T > 40$ km show an opposite seasonal cycle with enhanced values in summer and lower in winter and spring due to non-geostrophic SSH gradients at 60 km scales in summer. The GS-NAC system shows, unlike most other regions, adjacent positive and negative or very low anomalies. These are the regions, where the observation-based estimate even shows an opposite seasonal cycle (Fig. 2a and 2b).

For the non-tidal run, the estimation works even better. While the differences between the estimate and the original in the GS-NAC system occur as well, differences in regions, times and scales where and when the respective scale is below the transition scale do not show up (not shown). The FMA and ASO anomalies in the non-tidal run show a spring-enhanced inverse cascade almost everywhere except in the GS-NAC and parts of the BMC systems (not shown). In summary, the estimation fails where the compuation of geostrophic flows from SSH-gradients fails. Moreover, the estimation fails in very zonal and strong current-systems like the GS east of its separation. Based on the latter, we assume that the fluxes are overestimated in similar energetic regions, such as the western Kuroshio or the core Agulhas region. Outside of these very energetic regions, the estimation works very well. Future research needs to address the question, why the estimation works and why it fails in the core of very strong currents.

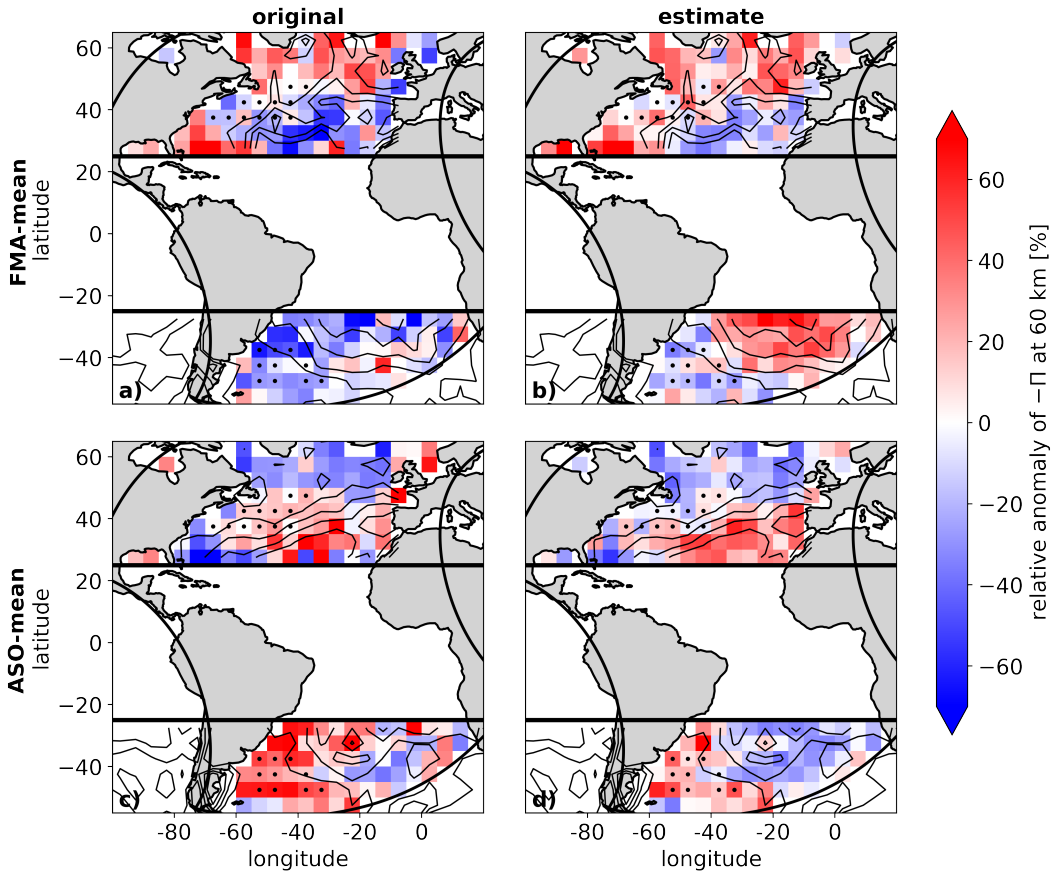

Figure 7. *The original (left) and the estimated (right) relative anomaly of the spring (FMA, top) and autumn (ASO, bottom) mean $-\Pi$ with respect to the 2008 annual mean at 70 km scales. Red (blue) colors mark an enhanced (reduced) inverse cascade. Dotted regions show where the $5° \times 5°$ averaged standard deviation of the AVISO-SSH in 2017-2021 is larger than 0.2 m. Contour lines mark where the maximum of the monthly climatology of T in the respective season is 40, 50, 60 and 70 km.*

References

1. Ferrari, R. & Wunsch, C. Ocean circulation kinetic energy: Reservoirs, sources, and sinks. *Annu. Rev. Fluid Mech.* **41**, 253–282 (2009).
2. Lévy, M. *et al.* Modifications of gyre circulation by sub-mesoscale physics. *Ocean. Model.* **34**, 1–15 (2010).
3. Hurlburt, H. E. & Hogan, P. J. Impact of 1/8° to 1/64° resolution on Gulf Stream model–data comparisons in basin-scale subtropical Atlantic Ocean models. *Dyn. Atmospheres Ocean.* **32**, 283–329 (2000).
4. Chassignet, E. P. & Xu, X. Impact of horizontal resolution (1/12° to 1/50°) on gulf stream separation, penetration, and variability. *J. Phys. Oceanogr.* **47**, 1999–2021 (2017).
5. Schubert, R., Gula, J. & Biastoch, A. Submesoscale flows impact Agulhas leakage in ocean simulations. *Commun. Earth & Environ.* **2**, 1–8 (2021).
6. Scott, R. B. & Wang, F. Direct evidence of an oceanic inverse kinetic energy cascade from satellite altimetry. *J. Phys. Oceanogr.* **35**, 1650–1666 (2005).
7. Molemaker, M. J., McWilliams, J. C. & Dewar, W. K. Submesoscale instability and generation of mesoscale anticyclones near a separation of the California Undercurrent. *J. Phys. Oceanogr.* **45**, 613–629 (2015).
8. Schubert, R., Schwarzkopf, F. U., Baschek, B. & Biastoch, A. Submesoscale impacts on mesoscale Agulhas dynamics. *J. Adv. Model. Earth Syst.* **11**, 2745–2767 (2019).
9. Jansen, M. & Ferrari, R. Macroturbulent equilibration in a thermally forced primitive equation system. *J. atmospheric sciences* **69**, 695–713 (2012).

10. Tulloch, R., Marshall, J., Hill, C. & Smith, K. S. Scales, growth rates, and spectral fluxes of baroclinic instability in the ocean. *J. Phys. Oceanogr.* **41**, 1057–1076 (2011).

11. Qiu, B., Chen, S., Klein, P., Sasaki, H. & Sasai, Y. Seasonal mesoscale and submesoscale eddy variability along the North Pacific Subtropical Countercurrent. *J. Phys. Oceanogr.* **44**, 3079–3098 (2014).

12. Wang, S., Liu, Z. & Pang, C. Geographical distribution and anisotropy of the inverse kinetic energy cascade, and its role in the eddy equilibrium processes. *J. Geophys. Res. Ocean.* **120**, 4891–4906 (2015).

13. Rhines, P. B. Waves and turbulence on a beta-plane. *J. Fluid Mech.* **69**, 417–443 (1975).

14. Capet, X., McWilliams, J. C., Molemaker, M. J. & Shchepetkin, A. Mesoscale to submesoscale transition in the California Current System. Part I: Flow structure, eddy flux, and observational tests. *J. Phys. Oceanogr.* **38**, 29–43 (2008).

15. Soh, H. S. & Kim, S. Y. Diagnostic characteristics of submesoscale coastal surface currents. *J. Geophys. Res. Ocean.* **123**, 1838–1859 (2018).

16. Schubert, R., Gula, J., Greatbatch, R. J., Baschek, B. & Biastoch, A. The submesoscale kinetic energy cascade: Mesoscale absorption of submesoscale mixed layer eddies and frontal downscale fluxes. *J. Phys. Oceanogr.* **50**, 2573–2589 (2020).

17. Balwada, D., Xie, J.-H., Marino, R. & Feraco, F. Direct observational evidence of an oceanic dual kinetic energy cascade and its seasonality . *arXiv preprint arXiv:2202.08637* (2022).

18. Garabato, A. C. N. *et al.* Kinetic energy transfers between mesoscale and submesoscale motions in the open ocean's upper layers. *J. Phys. Oceanogr.* **52**, 75–97 (2022).

19. Qiu, B., Nakano, T., Chen, S. & Klein, P. Bi-Directional Energy Cascades in the Pacific Ocean From Equator to Subarctic Gyre. *Geophys. Res. Lett.* **49**, e2022GL097713 (2022).

20. Leonard, A. Energy cascade in large-eddy simulations of turbulent fluid flows. In *Advances in geophysics*, vol. 18, 237–248 (Elsevier, 1975).

21. Germano, M. Turbulence: the filtering approach. *J. Fluid Mech.* **238**, 325–336 (1992).

22. Eyink, G. L. Locality of turbulent cascades. *Phys. D: Nonlinear Phenom.* **207**, 91–116 (2005).

23. Aluie, H., Hecht, M. & Vallis, G. K. Mapping the energy cascade in the North Atlantic Ocean: the coarse-graining approach. *J. Phys. Oceanogr.* **48**, 225–244 (2018).

24. Steinberg, J. M., Cole, S. T., Drushka, K. & Abernathey, R. P. Seasonality of the Mesoscale Inverse Cascade as Inferred from Global Scale-Dependent Eddy Energy Observations. *J. Phys. Oceanogr.* (2022).

25. Contreras, M., Renault, L. & Marchesiello, P. Understanding Energy Pathways in the Gulf Stream. *J. Phys. Oceanogr.* (2022).

26. Srinivasan, K., Barkan, R. & McWilliams, J. C. A forward energy flux at submesoscales driven by frontogenesis. *J. Phys. Oceanogr.* **53**, 287–305 (2023).

27. Storer, B. A., Buzzicotti, M., Khatri, H., Griffies, S. M. & Aluie, H. Global energy spectrum of the general oceanic circulation. *Nat. communications* **13**, 1–9 (2022).

28. Vergara, O., Morrow, R., Pujol, M.-I., Dibarboure, G. & Ubelmann, C. Global submesoscale diagnosis using along-track satellite altimetry. *Ocean. Sci.* **19**, 363–379 (2023).

29. Lahaye, N., Gula, J. & Roullet, G. Sea surface signature of internal tides. *Geophys. Res. Lett.* **46**, 3880–3890 (2019).

30. Lawrence, A. & Callies, J. Seasonality and spatial dependence of meso-and submesoscale ocean currents from along-track satellite altimetry. *J. Phys. Oceanogr.* (2022).

31. Qiu, B. *et al.* Seasonality in Transition Scale from Balanced to Unbalanced Motions in the World Ocean. *J. Phys. Oceanogr.* **48**, 591–605 (2018).

32. Xu, Y. & Fu, L.-L. The effects of altimeter instrument noise on the estimation of the wavenumber spectrum of sea surface height. *J. Phys. Oceanogr.* **42**, 2229–2233 (2012).

33. Dufau, C., Orsztynowicz, M., Dibarboure, G., Morrow, R. & Le Traon, P.-Y. Mesoscale resolution capability of altimetry: Present and future. *J. Geophys. Res. Ocean.* **121**, 4910–4927 (2016).

34. Klein, P. *et al.* Ocean-scale interactions from space. *Earth Space Sci.* **6**, 795–817 (2019).

35. Gula, J., Theetten, S., Cambon, G. & Roullet, G. Description of the GIGATL simulations, DOI: 10.5281/zenodo.4948523 (2021).

36. Shchepetkin, A. & McWilliams, J. C. The Regional Oceanic Modeling System (ROMS): A split-explicit, free-surface, topography-following- coordinate ocean model. *Ocean. Meteorol.* **9**, 347–404 (2005).

37. Arakawa, A. & Lamb, V. R. Computational design of the basic dynamical processes of the UCLA general circulation model. *Gen. circulation models atmosphere* **17**, 173–265 (1977).

38. Carton, J. & Giese, B. A reanalysis of ocean climate using Simple Ocean Data Assimilation (SODA). *Mon. Weather. Rev.* **136**, 2999–3017 (2008).

39. Renault, L., Masson, S., Arsouze, T., Madec, G. & McWilliams, J. C. Recipes for how to force oceanic model dynamics. *J. Adv. Model. Earth Syst.* **12**, e2019MS001715 (2020).

Acknowledgements

The authors gratefully acknowledges support from the French National Agency for Research (ANR) through the project DEEPER (ANR-19-CE01-0002-01). J.G. further gratefully acknowledges support from ISblue "Interdisciplinary graduate school for the blue planet" (ANR-17- EURE-0015).

Author contributions

R.S. and J.G. designed the study. J.G. performed the numerical model simulations. O.V. computed the monthly climatology of the transition scale from balanced to unbalanced flows. R.S. developed and executed all other analysis, produced the figures and wrote the text. J.G. and O.V. contributed to the discussion of the results and the writing of the manuscript.

Competing interests

The authors declare no competing interests.